Supplementary Information for

Promoting H_2O_2 Production via Molten-Salt-Engineered Carbon Nitride Photocatalyst in a Triphasic Membrane Reactor

Zirui You[1,#], Chuyue Lu[1,#], Jinpeng Hu[1], Xinxing Li[1], Jijia Sun[1], Yucong Huang[1], Fangrun Jin[1], Guanwu Lian[1], Wenguang Tu[1], Oleksandr Savateev[2], Jingjing Xiong[1,*], Dongxu Ji[1,*], Zhigang Zou[1], Zhongxin Chen[1,*]

[#] These authors contributed equally to this work. [*] Correspondence and requests for materials should be addressed to J. Xiong (jingjxiong@cuhk.edu.cn), D. Ji (jidongxu@cuhk.edu.cn), and Z. Chen (chenzhongxin@cuhk.edu.cn)

[1] Guangdong Basic Research Center of Excellence for Aggregate Science, School of Science and Engineering, The Chinese University of Hong Kong, Shenzhen, Guangdong, 518172, China.

[2] Department of Chemistry, The Chinese University of Hong Kong, Hong Kong, China.

Supplementary Methods

Instruments: X-ray diffraction (XRD) data were collected using a Rigaku Smartlab with Cu K_α radiation (40 kV, 40 mA). Scanning electron microscopy (SEM) images were captured with an MAIA 3 LMH at 12 kV, which is equipped with an energy-dispersive spectrometer (EDS) for elemental composition analysis. Fourier transform infrared spectroscopy (FTIR) spectra were measured by a PerkinElmer Spectrum Two™ FTIR spectrometer. The electrochemical measurement was performed using a Corrtest multichannel potentiostat, model CS310X. Rotational ring-disk electrode (RRDE) data were measured by a Corrtest multichannel potentiostat CS310X, combined with a Modulated Speed Rotator from Pine Research Instrument. O_2 temperature-programmed desorption (O_2-TPD) measurements were conducted using a Micromeritics AutoChem II 2920. X-ray photoelectron spectroscopy (XPS) and valence band XPS (VBXPS) data were collected by Thermo Scientific K-Alpha. High-resolution transmission electron microscopy (HRTEM) images were captured by JEOL JEM-F200. Photoluminescence and time-resolved photoluminescence spectra were obtained by using Edinburgh FLS1000. Mercury intrusion porosimetry measurement was conducted with Micromeritics AutoPore IV 9510.

Quantitative Determination of H_2O_2 using Iodometry: The concentration of H_2O_2 was measured by a typical iodometry method. In detail, 0.2 mL of potassium iodide aqueous solution (KI, 0.4 M) and 0.2 mL of potassium hydrogen phthalate aqueous solution ($HOOCC_6H_4COOK$, 0.1 M) were added to the sample solution with a dilution factor of 15 times. After at least 2 hours, the H_2O_2 concentration was determined by

measuring its absorbance at 351 nm using UV-vis spectroscopy via external standards. The standard calibration curve for H_2O_2 concentration is provided in **Figure S2**.

Photoelectrochemical Characterization: The electrochemical measurement was carried out with a Corrtest multichannel potentiostat CS310X in a conventional three-electrode cell, with a glassy carbon electrode (working electrode), a Pt plate (counter electrode), and an Ag/AgCl reference electrode. The catalyst inks were prepared by dispersing 10 mg of catalyst in 50 μL of Nafion, 475 μL of ethanol, and 475 μL of water. Then, 10 μL of catalyst ink was extracted and evenly coated onto a glassy carbon electrode with a diameter of 3 mm. 0.5 M Na_2SO_4 was used as the electrolyte. The electrochemical impedance spectroscopy (EIS) and the photocurrent tests were carried out under the irradiation of a Xenon light source (300 W). The following formula is applied to convert potential *vs.* Ag/AgCl to potential *vs.* RHE at room temperature:

$$E_{RHE} = E_{Ag/AgCl} + E^{0}_{Ag/AgCl\ vs.\ RHE} + 0.591 * pH = E_{Ag/AgCl} + 0.197\ V + 0.4137\ V$$

Fabrication of Mixed Matrix MS *g*-CN Membrane:

A mixed matrix MS *g*-CN membrane was prepared by solvent-induced phase separation. Typically, 265 mg of polyvinylidene fluoride (PVDF) and 45 mg of MS *g*-CN catalysts were dissolved in 10 mL of N-methyl-2-pyrrolidone (NMP) solvent. After two hours of stirring at 60 °C, 700 mg of PVDF was added. A mixed matrix MS *g*-CN membrane was then fabricated by the blade casting method onto a glass plate.

Apparent Quantum Yields (AQYs): AQYs were obtained using LED lights at various wavelengths (365, 420, 450, 485, 520, and 630 nm). The calculation is given by [12]

$$AQY = \frac{2n}{N_{aph}} \times 100\% = \frac{2MN_A\hbar c}{PSt\lambda} \times 100\%$$

where M is the number of H_2O_2 molecules in mole, N_A is the Avogadro's constant (6.022×10^{23} mol^{-1}), $\hbar$ is the Planck's constant (6.626×10^{-34} J·s), c is the speed of light (3×10^{8} m s^{-1}), P is the light intensity (50 mW cm^{-2}), S is the irradiation area (11.341 cm^2 with a diameter of 3.8 cm), and λ is the wavelength of the light in meters.

For example, under the irradiation of blue light (450 nm) for 30 min, $M = 3.608\ mM \times 25\ mL = 9.02 \times 10^{-5}\ mol$, then AQY was calculated as follows:

$$Apparent\ Quantum\ Yield\ (AQY) = \frac{2 * (9.02 \times 10^{-5} mol) * (6.022 \times 10^{23} mol^{-1}) * (6.626 \times 10^{-}}{(0.05 W/cm^2) * (11.341\ cm^2) * (1800 s) * (450 \times} = 6.062\%$$

In-situ FTIR Measurement: In situ diffuse reflectance infrared Fourier transform spectroscopy (DRIFTS) was conducted on a Bruker INVENIO S FTIR spectrometer (Germany) equipped with an MCT detector, using a Harrick in situ diffuse-reflectance reaction chamber operated in DRIFT mode. Photo-irradiation was supplied by a 300 W xenon lamp and directed into the chamber to illuminate the sample during spectral acquisition.

Computational Fluid Dynamics (CFD) Simulation: A two-dimensional layered porous media model was constructed in COMSOL Multiphysics to investigate the counterflow behavior of oxygen and water in a macroporous/microporous composite structure. As illustrated in **Figure S1**, the model comprises a macroporous layer on top and a microporous layer underneath. The geometric parameters, operating conditions,

and material properties used in the simulations are summarized in **Table S1.** The thicknesses of the macroporous and microporous layers were set to H_{mac} = 150 μm and H_{mic} = 30 μm, respectively, and the total model width was defined as W = 500 μm. This width was chosen to include a sufficient number of macropores and micropores, ensuring that the resulting gas-liquid interface distributions are statistically representative.

In the model, water was introduced from the top boundary, while oxygen was supplied from the bottom boundary, forming a counterflow configuration. The average pore sizes of the macroporous and microporous layers were d_{mac} = 57 μm and d_{mic} = 1.51 μm, respectively, with a porosity of 0.5 for both layers. These geometric parameters, together with the contact angles of each layer, were obtained from experimental measurements, while the model width was defined based on numerical considerations. The pore structures were generated using a random distribution algorithm under the prescribed geometric constraints, and a representative geometry was consistently applied across all simulations.

To simplify the problem and focus on the evolution of the gas–liquid interface in layered porous media, the following assumptions were adopted in the numerical model:

(1) Both gas and liquid phases were treated as incompressible fluids, and density variations during the flow process were neglected.

(2) All simulations were conducted under isothermal conditions with the temperature fixed at 298.15 K, and the effects of temperature variations on fluid properties,

including density, viscosity, and surface tension, were not considered.

(3) Given that the characteristic length scale of the porous structures is on the order of micrometers, capillary forces dominate the flow behavior; therefore, gravitational effects on the two-phase flow and interfacial morphology were neglected.

(4) The model focuses exclusively on the hydrodynamics and interfacial evolution of the gas-liquid system, without considering phase change, dissolution, or chemical reactions.

Based on these assumptions, a laminar two-phase flow framework was employed to describe the counterflow of oxygen and water within the layered porous media. Water was introduced from the top boundary, while oxygen was supplied from the bottom boundary. Constant pressure boundary conditions were applied at the top and bottom boundaries, and all remaining boundaries were treated as no-slip walls. Initially, the entire computational domain was filled with the gas phase.

The laminar two-phase flow was simulated using the level set method to track the gas–liquid interface. The flow field satisfies the continuity equation,

$$\nabla \cdot \mathbf{u} = 0 \qquad \text{* MERGEFORMAT (1.1)}$$

and the incompressible Navier–Stokes equation,

$$\rho\left(\frac{\partial \mathbf{u}}{\partial t} + \mathbf{u} \cdot \nabla \mathbf{u}\right) = -\nabla p + \nabla \cdot \left[\mu\left(\nabla \mathbf{u} + (\nabla \mathbf{u})^T\right)\right] + \mathbf{F}_{st} \text{*}$$

MERGEFORMAT (1.2)

where u is the velocity vector, and p is the pressure. The density ρ and viscosity μ depend on the local phase distribution and were calculated using the level set function ϕ:

$$\rho = \phi\rho_l + (1-\phi)\rho_g \qquad \text{* MERGEFORMAT (1.3)}$$

$$\mu = \phi\mu_l + (1-\phi)\mu_g \qquad \text{* MERGEFORMAT (1.4)}$$

where the subscripts l and g denote the liquid and gas phases. The interface motion is described by the level set equation,

$$\frac{\partial\phi}{\partial t} + \mathbf{u}\cdot\nabla\phi = \gamma_{ls}\nabla\cdot\left(\epsilon_{ls}\nabla\phi - \phi(1-\phi)\mathbf{n}\right)\text{*}$$

MERGEFORMAT (1.5)

where ϕ is the level set function, ϵls is the interface thickness parameter, γls is the reinitialization parameter, and n is the unit normal vector.

The bottom boundary of the model was set as the oxygen inlet, with a pressure of 1 atm, while the top boundary was set as the water inlet, also at a pressure of 1 atm. All other boundaries were treated as no-slip walls. The whole domain was initially filled with the gas phase. Water and oxygen were then introduced from the top and bottom boundaries, respectively. Gravity was neglected in all simulations.

Supplementary Figures

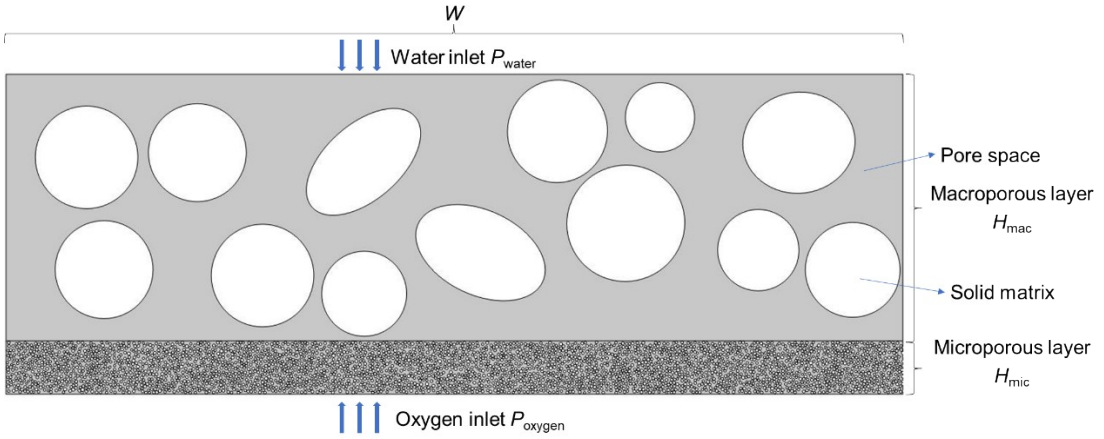

Figure S1. Schematic diagram of the layered porous media model used in the simulations.

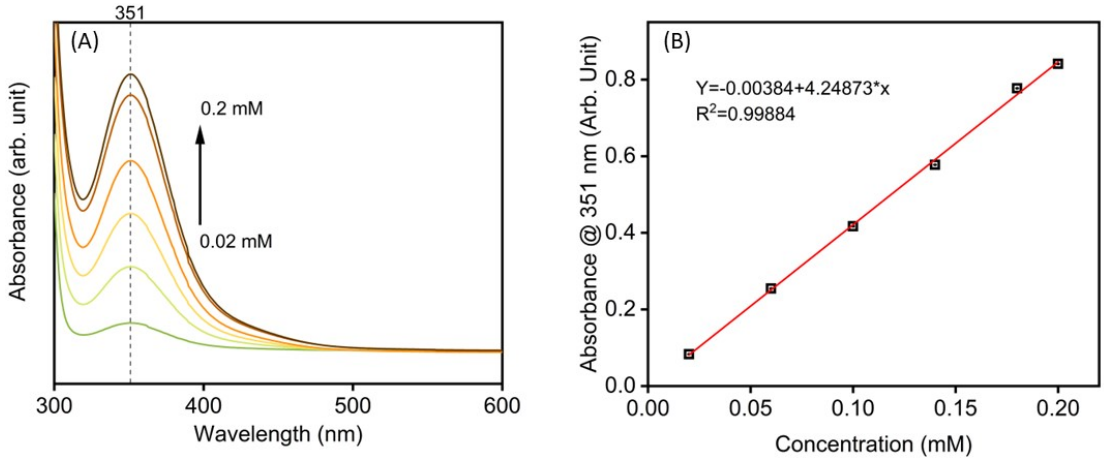

Figure S2. Iodometry determination of H_2O_2 concentration. (A) UV-Vis absorption spectra; (B) Calibration curve of the maximum absorption at 351 nm used for concentration determination.

The photocatalyst powder was dispersed in 25 mL of 10% aqueous isopropanol and irradiated for a random reaction time. A 1 mL aliquot of the same reaction batch was taken after the reaction. The original H_2O_2 concentration (C_{origin}) was determined directly by the iodometric method. Before measuring the second aliquot, 1 mL of a

standard H_2O_2 solution was added. Based on the known original concentration and the added standard concentration, we calculated the theoretical H_2O_2 concentration after mixing ($C_{calculated}$) and compared it with the measured concentration (C_{test}). The apparent recovery was therefore calculated:

$$\textbf{Recovery (\%)} = [1 - |C_{test} - C_{calculated}| / C_{calculated}] \times 100$$

Three independent tests using this method yielded recovery values of 91.7%, 93.2%, and 91.6%, respectively, for an average recovery of 92.2%. The results of this study indicate that the iodometric method provides acceptable analytical accuracy for measuring H_2O_2 over the concentration range relevant to this study. During UV-vis analysis, the absorbance was always maintained below 1.0 to ensure that the Beer-Lambert law remained valid within the linear response range. For the higher H_2O_2 concentrations, corresponding dilutions were performed before measurement.

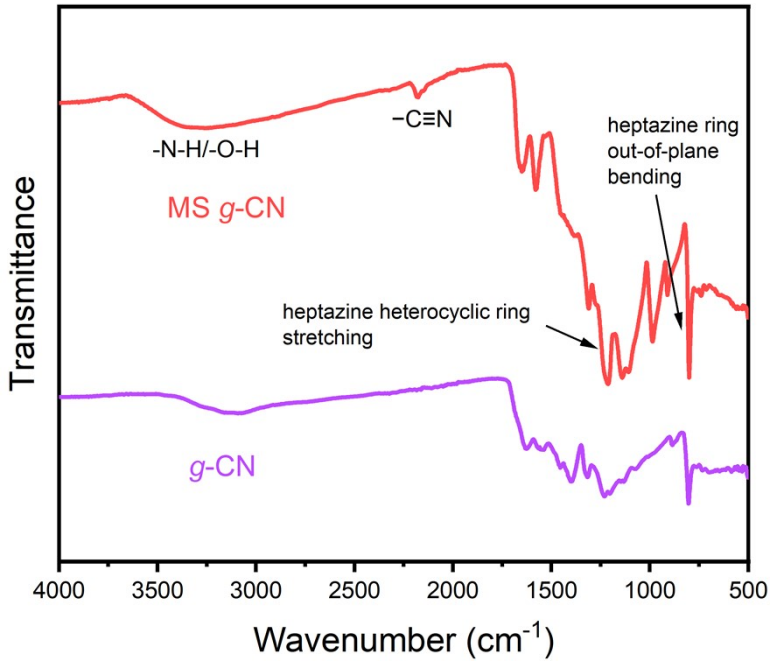

Figure S3. FTIR spectra of *g*-CN and MS *g*-CN photocatalysts.

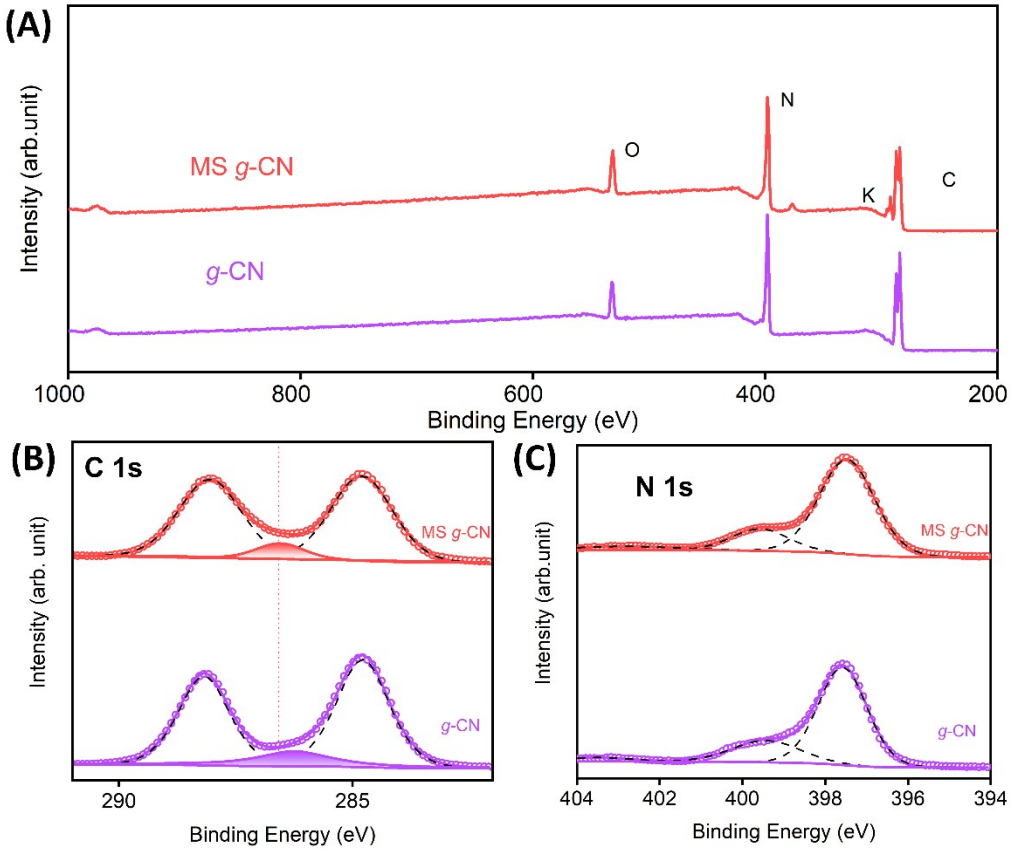

Figure S4. XPS spectra of the pristine *g*-CN and MS *g*-CN photocatalysts. (A) Survey, (B) C 1s core-level, and (C) N 1s core-level spectra.

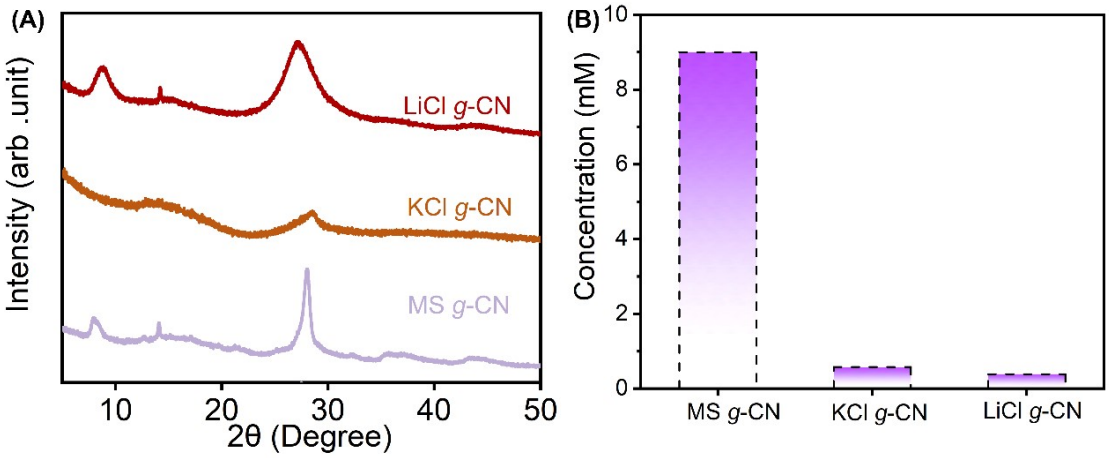

Figure S5. Eutectic molten-salt treatment outperforms single-salt treatment in (A) structural regulation and (B) photocatalytic performance of *g*-CN.

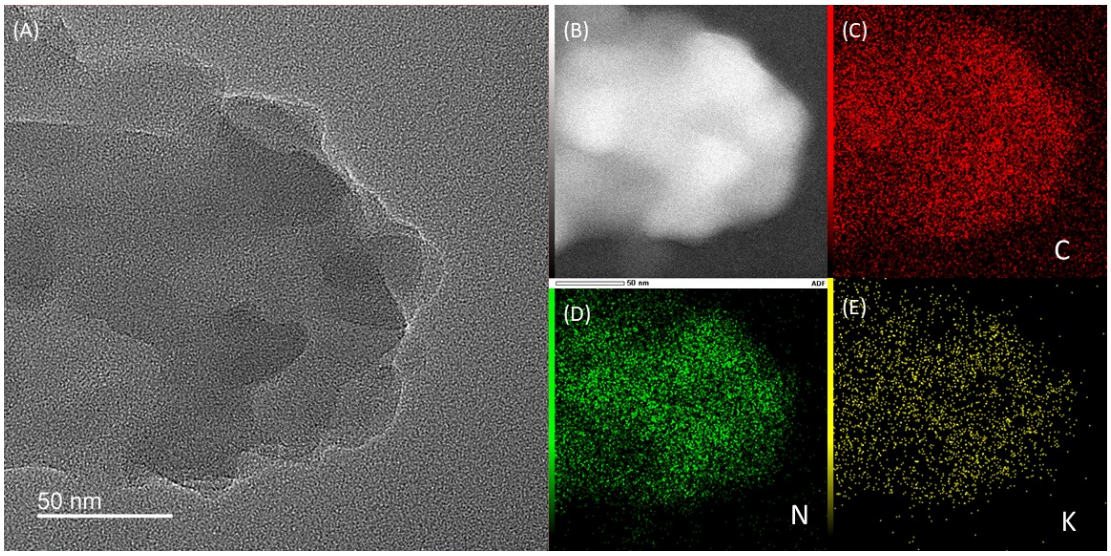

Figure S6. HRTEM morphology of the MS *g*-CN photocatalyst. (A) HRTEM image, (B-E) the corresponding EDS mappings.

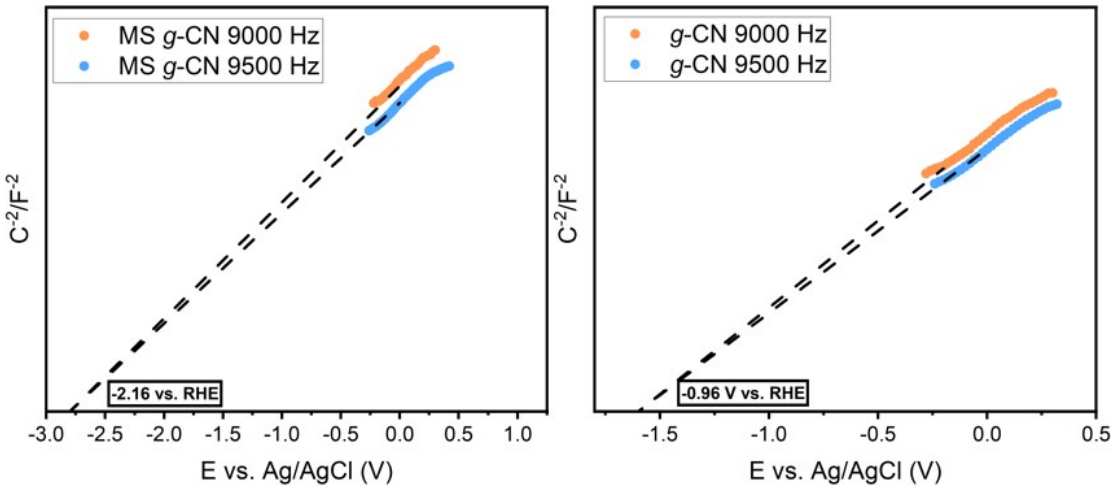

Figure S7. Mott-Schottky plots of (a) MS *g*-CN and (b) *g*-CN photocatalysts.

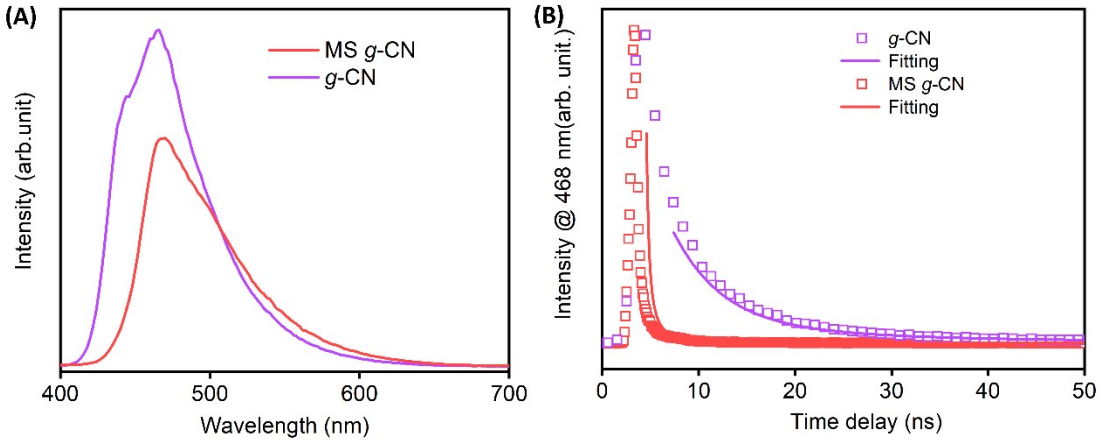

Figure S8. (A) PL and (B) TRPL spectra of the pristine *g*-CN and MS *g*-CN.

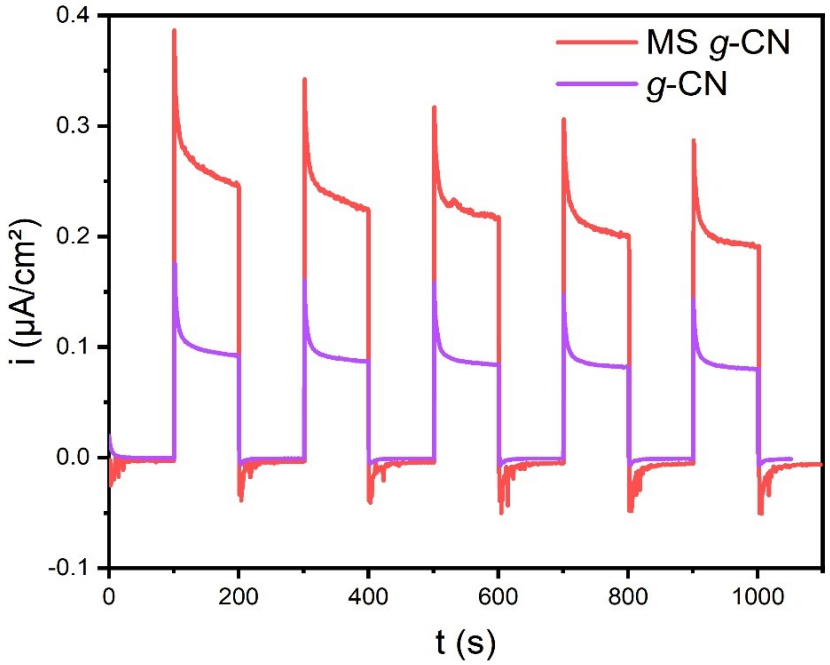

Figure S9. Transient photocurrent responses of pristine *g*-CN and MS *g*-CN.

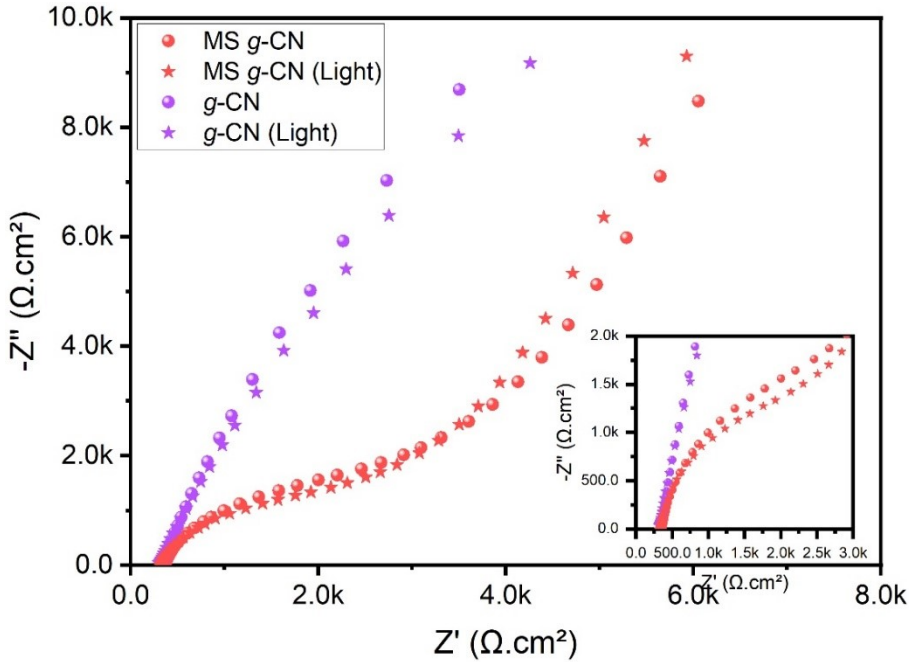

Figure S10. Electrochemical impedance spectra of *g*-CN and MS *g*-CN photocatalysts in the dark and in the light. The inset shows the enlarged area in the charge-transfer region.

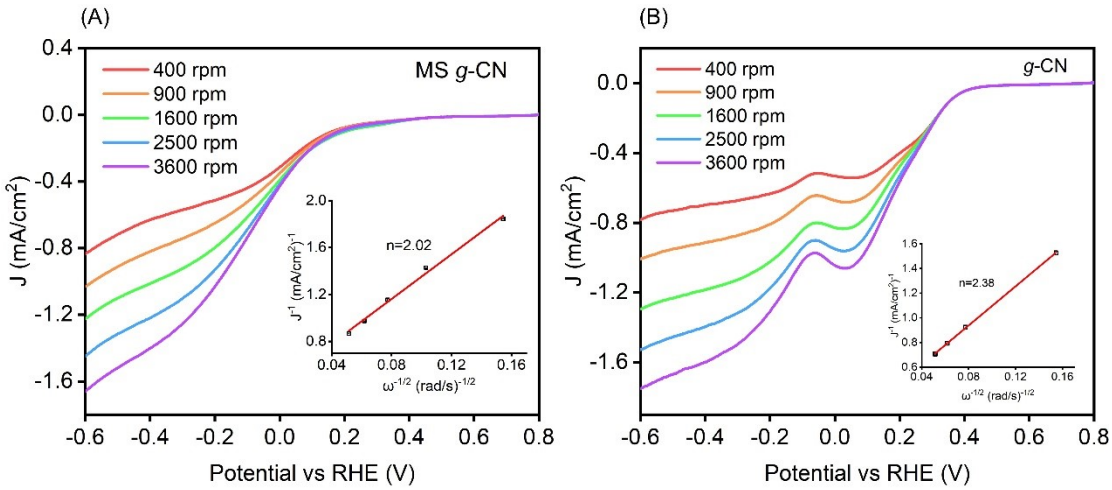

Figure S11. RDE linear sweep voltammograms of the oxygen reduction reaction on **(A)** MS *g*-CN and **(B)** pristine *g*-CN recorded at rotation rates of 400–3600 rpm, shown as current density (j) versus potential (vs RHE). **Insets:** corresponding Koutecky–Levich (K–L) plots used to determine the electron transfer number (n), yielding n = 2.02 for MS *g*-CN and n = 2.38 for *g*-CN.

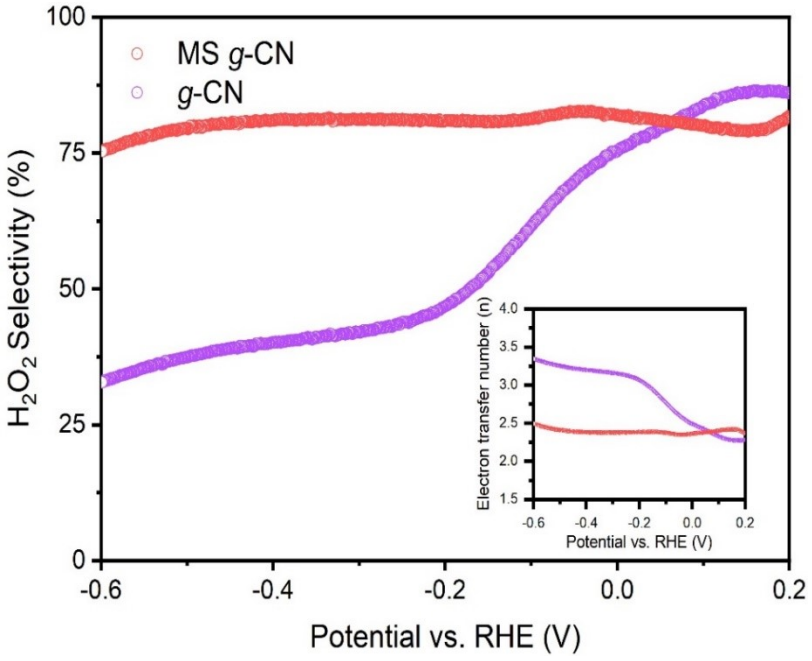

Figure S12. The H_2O_2 selectivity of pristine *g*-CN and MS *g*-CN, with an inset showing the number of electrons transferred.

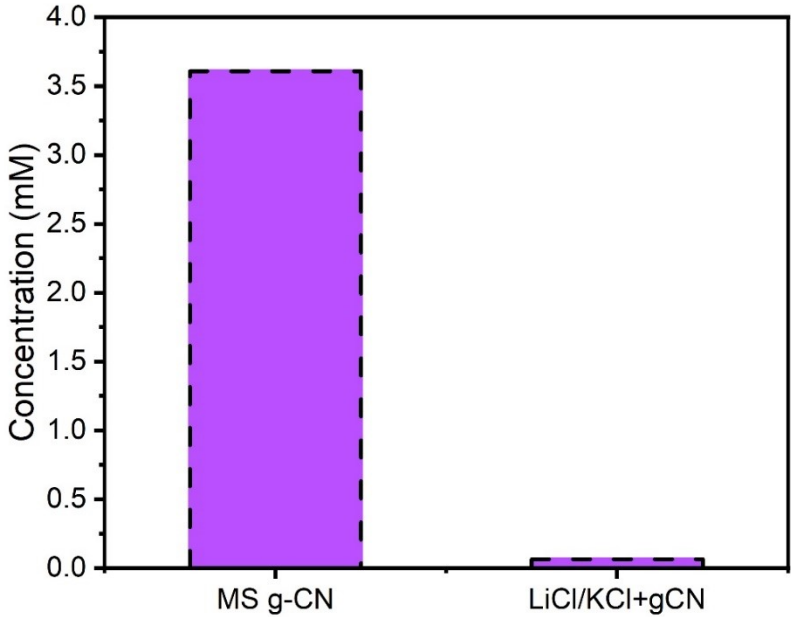

Figure S13. Comparison of the performance of MS *g*-CN and pristine *g*-CN, together with LiCl and KCl.

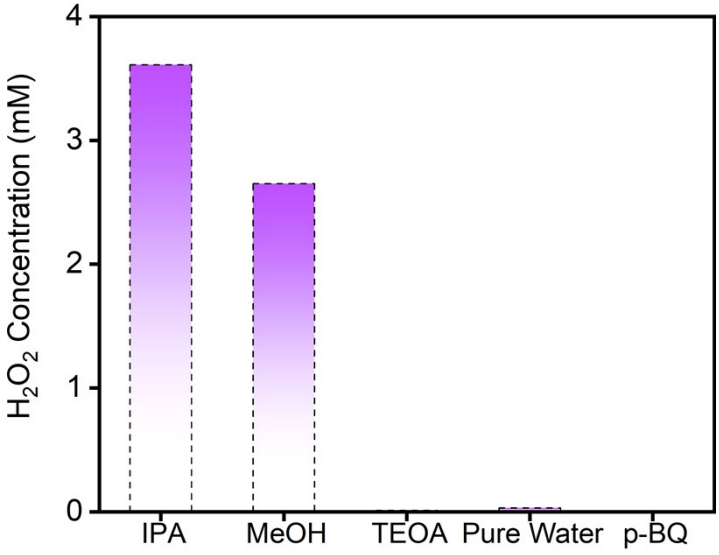

Figure S14. Photocatalytic H_2O_2 production of MS *g*-CN using various sacrificial agents at 450 nm.

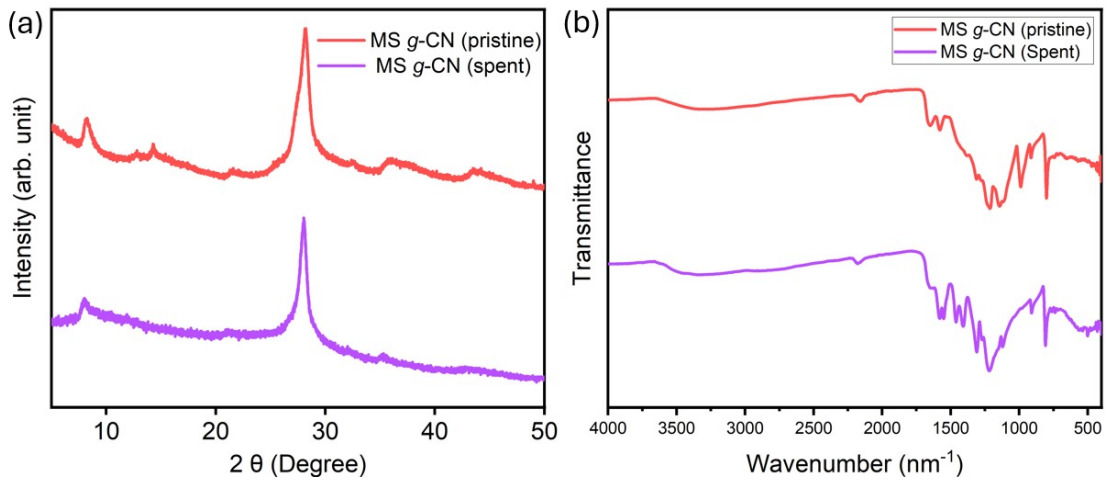

Figure S15. (a) XRD patterns and (b) FTIR spectra of the pristine and spent MS *g*-CN photocatalysts after five catalytic cycles.

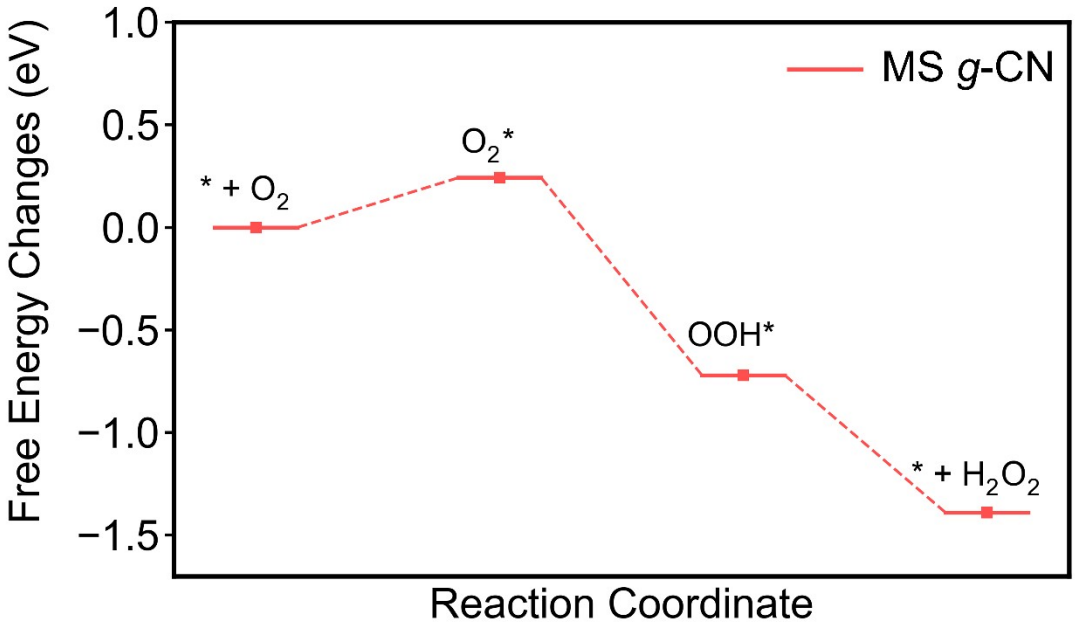

Figure S16. DFT-calculated reaction coordinates over the MS *g*-CN catalyst. No favorable O_2 adsorption was observed over the pristine *g*-CN catalyst.

$$\text{MS g-CN} + h\nu \rightarrow e^-_{CB} + h^+_{VB}$$

$$(CH_3)_2CHOH + h^+_{VB} \rightarrow (CH_3)_2C\bullet OH + H^+$$

$$(CH_3)_2C\bullet OH + O_2 \rightarrow (CH_3)_2C(OH)OO\bullet$$

$$(CH_3)_2C(OH)OO\bullet \rightarrow (CH_3)_2C{=}O + HO_2\bullet$$

$$HO_2\bullet \rightarrow H_2O_2 + O_2$$

or

$$HO_2\bullet + e^-_{CB} + H^+ \rightarrow H_2O_2$$

Figure S17. Proposed mechanism of photocatalytic H_2O_2 production using MS *g*-CN.

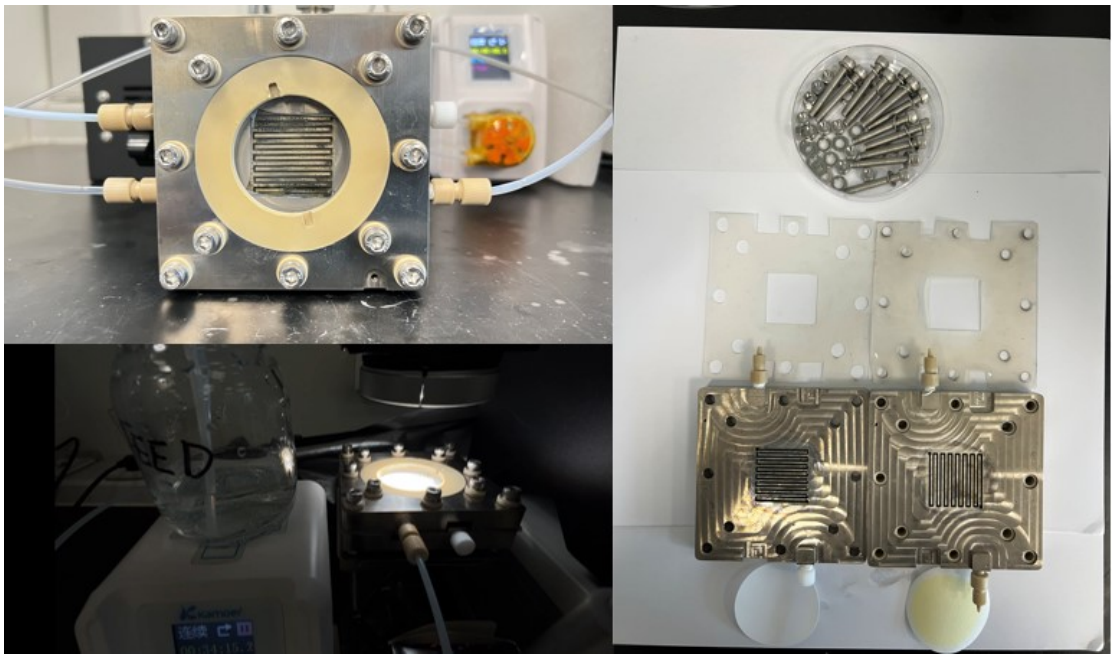

Figure S18. Photos of the 9 cm^2 flow membrane reactor. The top left image shows the assembled reactor. The bottom left image illustrates the reactor in operation with illumination. The right image presents a disassembled view of the various components.

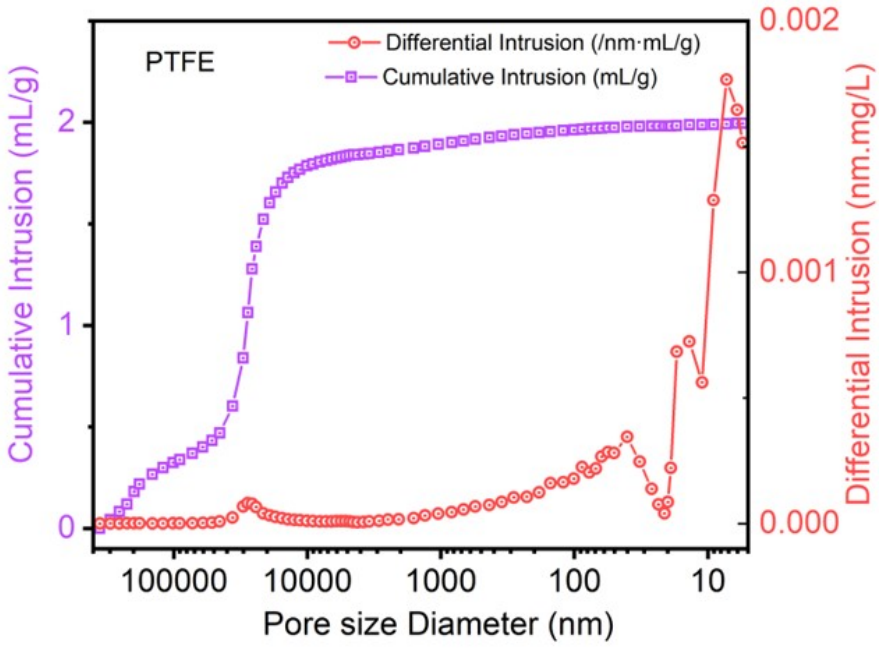

Figure S19. Mercury intrusion porosimetry of the pure PTFE membrane.

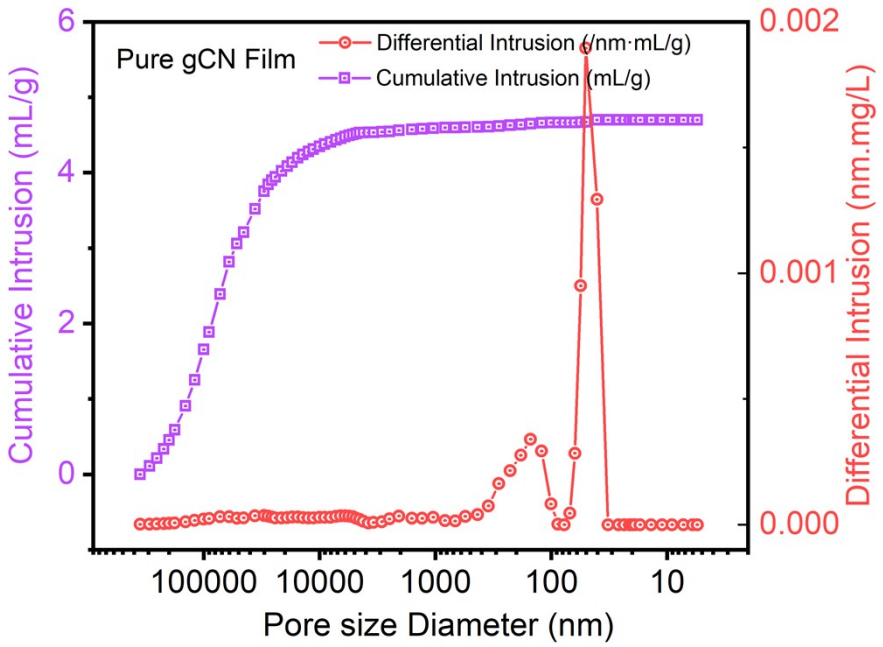

Figure S20. Mercury intrusion porosimetry of the mixed matrix MS *g*-CN membrane (without PTFE backings).

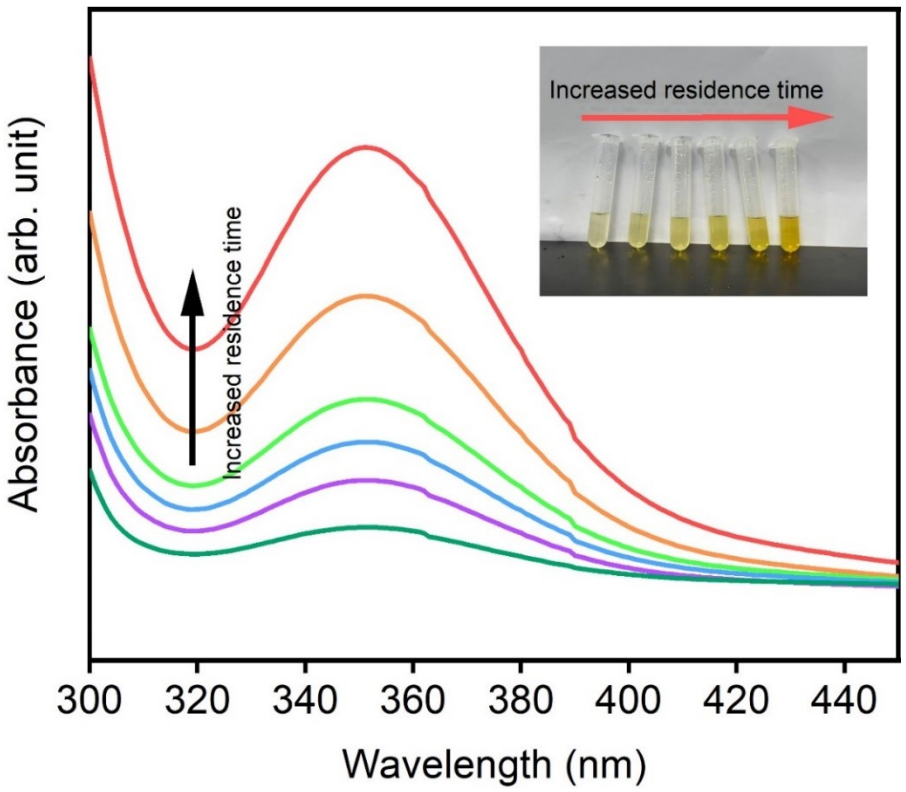

Figure S21. Concentration of H_2O_2 generated at different residence times (*i.e.*, different flow rates) using the MS *g*-CN/PTFE membrane catalyst.

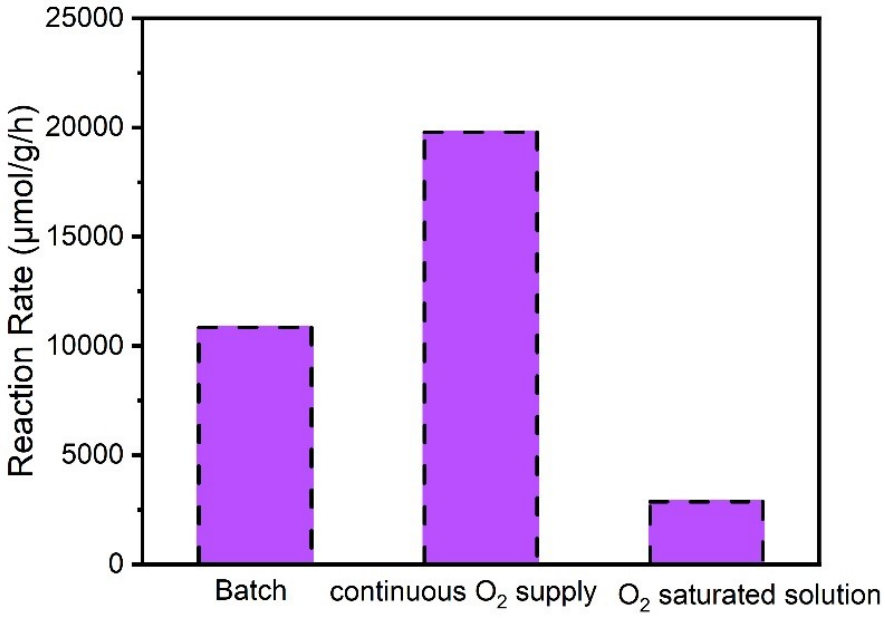

Figure S22. The influence of oxygen diffusion pathways on reactor performance.

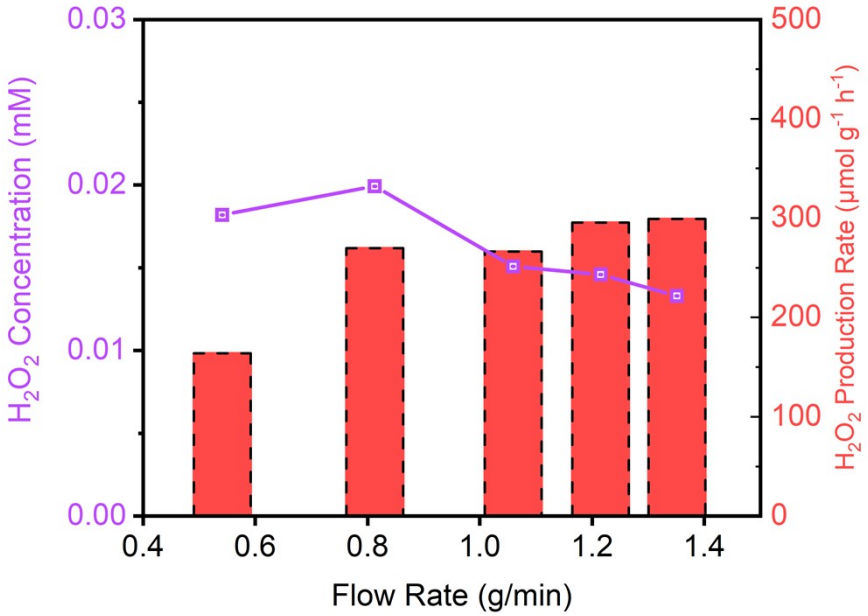

Figure S23. Continuous-flow production of H_2O_2 using the MS *g*-CN/PTFE membrane in a 9 cm^2 triphasic membrane reactor without adding IPA as the sacrificial agent under white light illumination.

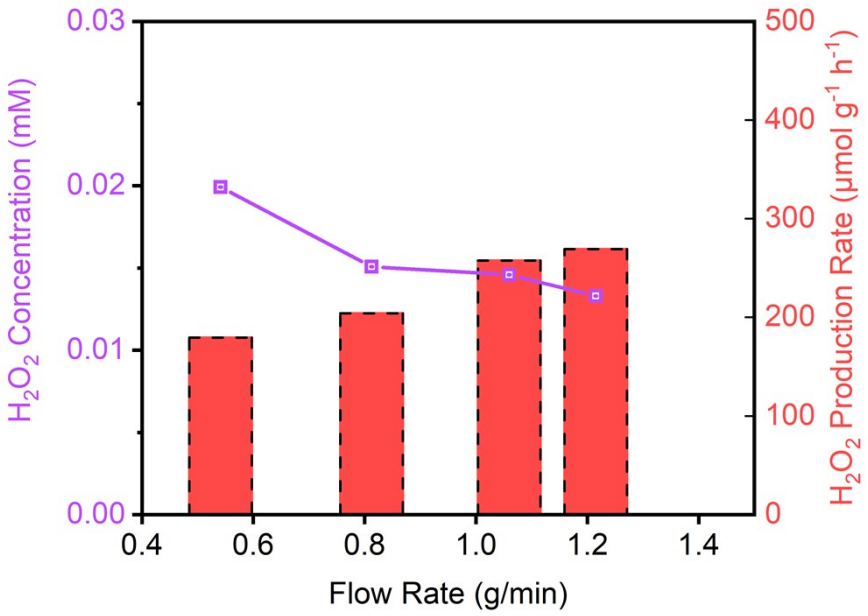

Figure S24. Continuous flow production of H_2O_2 using the mixed matrix MS *g*-CN membrane (without PTFE backings) in a 9 cm^2 triphasic membrane reactor under white light illumination.

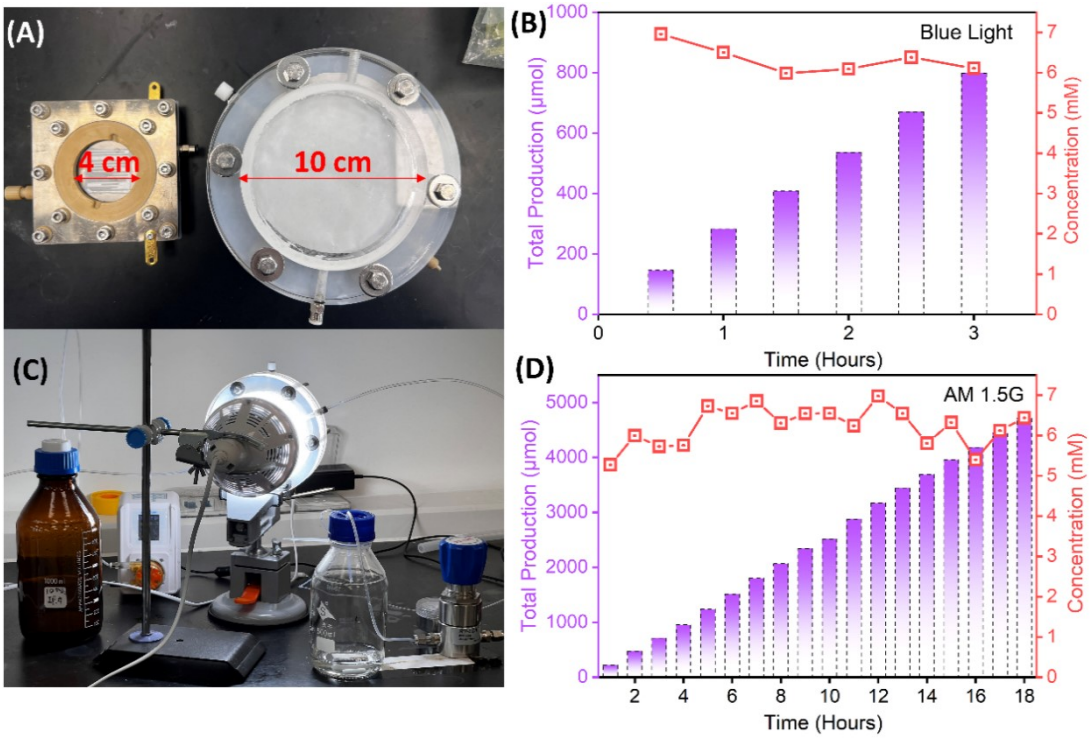

Figure S25. Scale-up of the membrane reactor for continuous H_2O_2 production. (A) Photograph comparing the original 4 cm-diameter reactor with the enlarged 10 cm-diameter reactor; (B) Time-dependent H_2O_2 production in the enlarged reactor under blue-light irradiation at XXX bar of O_2; (C) Photograph of the enlarged membrane reactor operating under reaction conditions with AM 1.5G simulated solar illumination; (D) Time-dependent H_2O_2 production in the 10 cm reactor under AM 1.5G irradiation at XXX bar of O_2, showing both productivity (left) and outlet concentration (right).

Supplementary Tables

Table S1. Recovery of the iodometric method used for H_2O_2 quantification

Sample	C_{origin}	C_{add}	$C_{calculated}$	C_{test}	Difference %
1	1.8	4.2	3.05	3.3	8.3
2	5.6	4.2	4.9	5.3	6.8
3	5.4	4.2	4.8	5.2	8.4

Table S2. Geometric parameters, operating conditions, and material properties used in the simulations.

Parameters	Value	Description
T	298.15 K	Temperature
H_{mac}	150 μm	Depth of macroporous layer
H_{mic}	30 μm	Depth of microporous layer
W	500 μm	Weight of geometry
P_{oxygen}	1 atm	O_2 inlet pressure
P_{water}	1 atm	Water inlet pressure
d_{mac}	57 μm	Average pore size of the Mac layer
d_{mic}	1.51 μm	Average pore size of the Mic layer
γ_{mac}	116.9°	Contact angle of the Mac layer
γ_{mic}	147°	Contact angle of the Mic layer
ε	0.5	Porosity
γ	0.072 N m^{-1}	Surface tension

Table S3. Performance tracker of carbon nitride-based catalysts on H_2O_2 production.

Catalyst	H_2O_2 Yield Rate ($\mu mol\ g^{-1}\ h^{-1}$)	Concentration (μM)	Sacrificial Agent	Electron Transfer (n)	Ref.
MS *g*-CN	**10,800**	**8,700**	**Isopropanol**	**2.0**	**Our work**
PCNHS	1,648	95	Isopropanol	2.2	11
g-C_3N_4/In_2S_3-10%	92	294	None	--	22
CoO_x-N_vCN	250	250	None	2.3	23
P-mMCNNS-25	1,083	3,249	Ethanol	--	24
B-*g*-C_3N_4-20	419	419	Isopropanol	--	25
CPCN	1,569	471	Ethanol	--	26
CN/CFS,N	1,318	1,600	Ethanol	1.0	27
NH_3-$NaClO_{0.5}$-CN_w	1,038	415	Ethanol	2.2	28
BCN400	600	400	Ethanol	2.0	29
DCN	351	352	Ethanol	--	30
SS-CN	567	275	Isopropanol	2.0	31
N4%/$O_{0.2}$tCN	2,464	1,230	Ethanol	2.2	32
O-CNC	2,008	4,000	Isopropanol	--	33
m-CNNP	43	43	Isopropanol	1.9	34
$CNCF_2$	1,100	1,100	Ethanol	1.7	35
CN-ND	200	85	Ethanol	--	36
CM-CN_3	150	150	Ethanol	--	37

Fl-CN-530	952	200	Ethanol	--	38
0.019Ru-TCN	296	300	Isopropanol	--	39
CN-HMoP-3	274	700	Ethanol	--	40
$CDs_{10}MCN$	423	1,480	Isopropanol	--	41
$Bi_{3.6}K_3$-CN	1,342	4,340	Ethanol	2.2	42
pCN1	707	3,500	Isopropanol	1.2	43
CN-0.5	73	300	Ethanol	--	44
CoP/Co@NPC /*g*-C_3N_4	940	563	Isopropanol	--	45
g-C_3N_4-0.05	704	2,750	Isopropanol	2.2	46
TC/CN-20	561	580	Ethanol	--	47
DPCN	2830	283	Ethanol	--	48

Table S4. Factors that affect performance in photocatalytic H_2O_2 generation.[1]

Run	Temperature (°C)	Sacrificial agent	Atmosphere	Performance (mmol $g_{catalyst}^{-1}$ h^{-1})
1	10	IPA	Air	4.67
2	20	IPA	Air	9.02
3	30	IPA	Air	12.80
4	40	IPA	Air	9.58
5	50	IPA	Air	5.31
6	20	None	O_2	0.42
7	20	None	Air	0.26
8	20	None	Ar	0.15

[1] Test condition: The experiment was conducted in a batch reaction. Typically, 20 mg of catalyst powder was dispersed in 25 mL of a 10 vol% IPA solution in Runs 1 ~ 5. The reaction system is the same for Runs 6 ~ 8, except for the removal of IPA. Blue light (450 nm) was used as the light source.